

DANISH METEOROLOGICAL INSTITUTE

—— SCIENTIFIC REPORT ——

03-11

**Quasigeostrophic interpretation of
extratropical cyclogenesis**

Niels Woetmann Nielsen



COPENHAGEN 2003

ISSN Nr. 0905-3263 (printed)
ISSN Nr. 1399-1949 (online)
ISBN-Nr. 87-7478-487-0

Quasigeostrophic interpretation of extratropical cyclogenesis

Niels Woetmann Nielsen
Danish Meteorological Institute, Copenhagen, Denmark

August 15, 2003

Abstract

Understanding of extratropical cyclogenesis has been a research theme right from the beginning of modern (scientifically based) meteorology, and unsolved problems related to cyclogenesis still remain. Major milestones in the understanding of extratropical cyclogenesis have been the development of the frontal cyclone model by Norwegian meteorologists around 1920 and the formulation by Charney in 1947 of the quasigeostrophic equations, which are consistent order of magnitude approximations to the governing atmospheric equations. In teaching meteorology much emphasis is usually put on the equations and solutions to the equations under idealized circumstances. Less attention is perhaps given to the physical interpretation of the equations. A broad spectrum of extratropical cyclogenesis events is observed in the atmosphere, ranging from 100 km-scale polar lows to more than 5000 km-scale cyclones. A very important property of extratropical cyclones is that they modify the background flow in which they evolve. Thereby they contribute to breed the ground for new (upstream and downstream) developments, not necessarily occurring on the same space and time scale. A clear understanding of the important physical processes in extratropical cyclogenesis is valuable in itself and very useful knowledge in dynamic conceptions of conventional weather observations, satellite images and numerical analyses and forecasts. The quasigeostrophic equations contain the coupling between dynamic and thermodynamic processes of fundamental importance in extratropical cyclogenesis. The coupling in the quasigeostrophic system is interpreted physically in a qualitative sense by making use of idealized examples. The interpretation is not restricted to explain ‘downstream of upper-level trough’ cyclogenesis as is the case in many textbooks on dynamic meteorology. It covers the entire life cycle of the surface cyclone and its associated upper-level wave-jet system. As an example a five day sequence of extratropical cyclone developments over the western North Atlantic is analyzed by using quasigeostrophic arguments. The sequence includes a polar low formation.

1. Introduction

Conversion of available potential energy (APE) into kinetic energy (KE) plays a central role in extratropical cyclogenesis. The deepening of an extratropical cyclone is primarily a result of the conversion of APE in the mean (or large scale) flow to KE in the deepening cyclone. The APE of the mean flow is continuously generated by large scale diabatic (primarily radiative) and advective processes.

The conversion of APE into KE of the cyclone leads to a lowering of the center of gravity of the air mass involved in the cyclogenesis. Therefore the three dimensional motions in a developing cyclone must be organized in such a way that cold air streams sink on average, whereas warm air streams rise on average. Release of latent heat, primarily in the rising warm and moist air streams of the developing cyclone usually intensifies the cyclogenesis. In some polar lows latent heat release may become the main energy source for the development.

Contrary to deep convective systems, such as cumulonimbi, the vertical motions in extratropical cyclones are much weaker (usually about two orders of magnitude) than the horizontal motions. Air particles that enter the cyclone near its bottom (sea or land surface) typically travel 1000 km or more before they leave the cyclone near its top (tropopause). The same holds for air particles that enter and leave the cyclone at its top and bottom, respectively. The extratropical cyclone is indeed a shallow phenomenon with an aspect ratio (vertical to horizontal dimension) of the order of 10^{-2} (10 km/1000 km). In comparison the aspect ratio of cumulonimbi typical is of the order of 1 (10 km/10 km).

Extratropical cyclogenesis is a kind of instability, involving positive feed-backs between advective and diabatic processes in the troposphere. The fundamental mechanisms in extratropical cyclogenesis are present in the quasigeostrophic approximations to the governing equations of the atmosphere. The mechanisms disappear if any further consistent approximations are made. In less restrictive, consistent approximations to the governing equations, the complexity of the equations increases and makes the physical interpretation much more difficult.

The present report gives a physical (and qualitative) interpretation of the quasigeostrophic equations with particular emphasis on the omega and geopotential tendency equations. The quasigeostrophic equations are presented in section 2 and 3. A qualitative physical interpretation of the omega and geopotential tendency equations are given in section 4.

Cyclogenesis related to wave dynamics is discussed in section 5 followed by a discussion of cyclogenesis related to jet stream dynamics in section 6. A five day sequence of extratropical cyclone developments over the western North Atlantic in February 2003, including a polar low formation, is analyzed in section 7. The sequence serves as an example of the use of quasigeostrophic thinking in dynamic conceptions of satellite images in combination with numerical analyses. Finally, section 8 contains discussion and conclusions.

2. Quasigeostrophic approximations

Usually the atmosphere can be considered to be in hydrostatic balance for motions on horizontal scales larger than 5 to 10 km. Hydrostatic balance implies that the ω -velocity (i.e. the vertical velocity in the pressure coordinate system) becomes the vertical velocity necessary to maintain conservation of mass in the atmosphere. It follows from mass continuity ($\frac{\partial u}{\partial x} + \frac{\partial v}{\partial y} + \frac{\partial w}{\partial p} = 0$) that ω is determined *diagnostically* from the (prognostic) horizontal wind field.

Horizontal motions in the atmosphere on synoptic scales larger than 1000 km also tend to be in near geostrophic balance. For such motions the geostrophic part of the

horizontal wind field tends to be an order of magnitude larger than the ageostrophic part. For such flows the Rossby number $Ro = V/f_0L$ tends to be of the order 0.1. Ro is the ratio between the magnitude of the nonlinear advection of horizontal momentum and the magnitude of the horizontal Coriolis force per unit mass. V and L is a representative advection velocity and horizontal length scale of the flow, respectively, and f_0 is the Coriolis parameter in the central part of the flow domain.

Atmospheric flow in nearly geostrophic balance is governed by the so called quasi-geostrophic equations (the QG equations) first derived by Charney (Charney, 1947). In addition to the hydrostatic balance the latter equations are midlatitude beta-plane approximations of the horizontal momentum and thermodynamic energy equations based on order of magnitude estimates of the terms in the equations. The QG equations for momentum and temperature are written in equation (1) and (2), respectively.

$$\frac{D_g \vec{V}_{g0}}{Dt} = -f_0 \vec{k} \times \vec{V}_a - \beta y \vec{k} \times \vec{V}_{g0} + \vec{F} \quad (1)$$

$$\frac{D_g T}{Dt} - \left(\frac{\sigma p}{R}\right) \omega = \frac{J}{c_p} \quad (2)$$

In these equations the rate of change of momentum and temperature following the motion are replaced by the rate of change of *geostrophic* momentum and temperature following the *geostrophic* motion, i.e. the operator

$$\frac{D}{Dt} = \frac{\partial}{\partial t} + \vec{V} \cdot \nabla_p \quad (3)$$

is replaced by

$$\frac{D_g}{Dt} = \frac{\partial}{\partial t} + \vec{V}_{g0} \cdot \nabla_p \quad (4)$$

V_{g0} is defined: $V_{g0} = f_0^{-1} \cdot \vec{k} \times \nabla_p \phi$, where \vec{k} is the vertical unit vector and $\phi = gz$ is the geopotential. This definition of the geostrophic wind implies $\nabla \cdot \vec{V}_{g0} = 0$ and if $\vec{V}_g = f^{-1} \cdot \vec{k} \times \nabla_p \phi$, the difference $\vec{V}_g - \vec{V}_{g0}$ becomes a part of the ageostrophic wind (see Appendix A). In (2) $\sigma = -RT_0 p^{-1} \partial \ln \theta_0 / \partial p$ is a (positive) static stability parameter and θ_0 is the potential temperature corresponding to the basic state temperature T_0 . For details about the derivation of (1) and (2), see Holton, 1992 (section 6.2).

3. The quasigeostrophic geopotential tendency and omega equations

In the QG system a horizontal ageostrophic wind field is necessary to retain balance in the QG equations in the same way as ω is necessary to retain hydrostatic balance. The horizontal ageostrophic wind field is determined *diagnostically* from the geostrophic wind field. If further the geostrophic wind is defined by a constant Coriolis parameter f_0 (implying a non-divergent geostrophic wind) it follows from the continuity equation that ω is determined by the ageostrophic part of the wind field. The latter wind field (including ω) is called the secondary circulation. Therefore, in the QG system the secondary circulation at any time is determined *diagnostically* from the *prognostic* geostrophic wind field (or equivalently from the geopotential field, since the geostrophic wind is proportional to the horizontal gradient (on a pressure surface) of the geopotential field).

Due to advection by the geostrophic wind, diabatic heating and friction, the geostrophic and hydrostatic balance is ceaselessly disturbed. The secondary circulation is at any moment the ageostrophic wind field that must be added to the geostrophic wind to retain QG balance (i.e. hydrostatic balance and the balance in (1) and (2)).

For a developing baroclinic system the secondary circulation always counteracts changes in the geopotential field generated by geostrophic advection, diabatic heating and friction. In cyclogenesis the counteracting effect of the secondary circulation does not completely eliminate changes in the geostrophic wind field imposed by advection, diabatic heating and friction. If the latter changes happens to be proportional to the geostrophic wind field, the latter must amplify exponentially with time provided that the constant of proportionality is positive. A large growth rate means a large constant of proportionality, and hence a rather inefficient counteracting capability of the secondary circulation.

Baroclinic growth (usually referred to as baroclinic instability) is therefore possible in the QG system. However, the instability is not as easy to understand as for example conditional instability. One way to obtain an idea about how the instability works is to consider the geopotential tendency equation and the ω -equation in the QG framework. These equations, shown below in (5) and (6), respectively, combine dynamics (equation (1)) and thermodynamics (equation (2)) in the QG system. The derivation is relatively straightforward and is described in for example Holton, 1992. (section 6.3 and 6.4). The result is:

$$(\nabla_p^2 + \frac{f_0^2}{\sigma} \frac{\partial^2}{\partial p^2})\chi = -f_0 \vec{V}_{g0} \cdot \nabla_p (\zeta_{g0} + f) - \frac{f_0^2}{\sigma} \frac{\partial}{\partial p} (-\frac{R}{p} \vec{V}_{g0} \cdot \nabla_p T), \quad (5)$$

$$(\nabla_p^2 + \frac{f_0^2}{\sigma} \frac{\partial^2}{\partial p^2})\omega = -\frac{f_0}{\sigma} \frac{\partial}{\partial p} (-\vec{V}_{g0} \cdot \nabla_p (\zeta_{g0} + f)) - \frac{R}{\sigma p} \nabla_p^2 (-\vec{V}_{g0} \cdot \nabla_p T). \quad (6)$$

In (5) $\chi = \partial\phi/\partial t$ is the geopotential tendency. For simplicity, friction and diabatic heating has been neglected in (5) and (6), and it has also been assumed that the static stability parameter σ is a (positive) constant. It can be shown that the effect of friction is similar to the effect of geostrophic vorticity advection. Therefore, the effect of friction can formally be included in the first forcing term on the right hand side (rhs) of (5) and (6). In the same way is the effect of diabatic heating similar to the effect of temperature advection. Formally it can therefore be included in the second forcing term on the rhs of (5) and (6). The QG equations (5) and (6) with friction and diabatic heating included are presented in e.g. Blustein, 1992.

For a qualitative discussion, as given here, it is convenient to write (5) and (6) in symbolic form. The operator $\nabla_p^2 + f_0^2/\sigma \partial^2/\partial p^2$ on the lhs of (5) and (6) is similar to the 3-dimensional Laplace operator. It can be shown that the Laplacian of a variable which can be written as a sum of sine and/or cosine functions, is proportional to minus the variable itself. In general the Laplacian of a local maximum and minimum is negative and positive, respectively. For the qualitative discussion given here we will therefore write the equations symbolically as

$$\chi \propto -f_0 VA + \frac{f_0^2}{\sigma} DTA \quad (7)$$

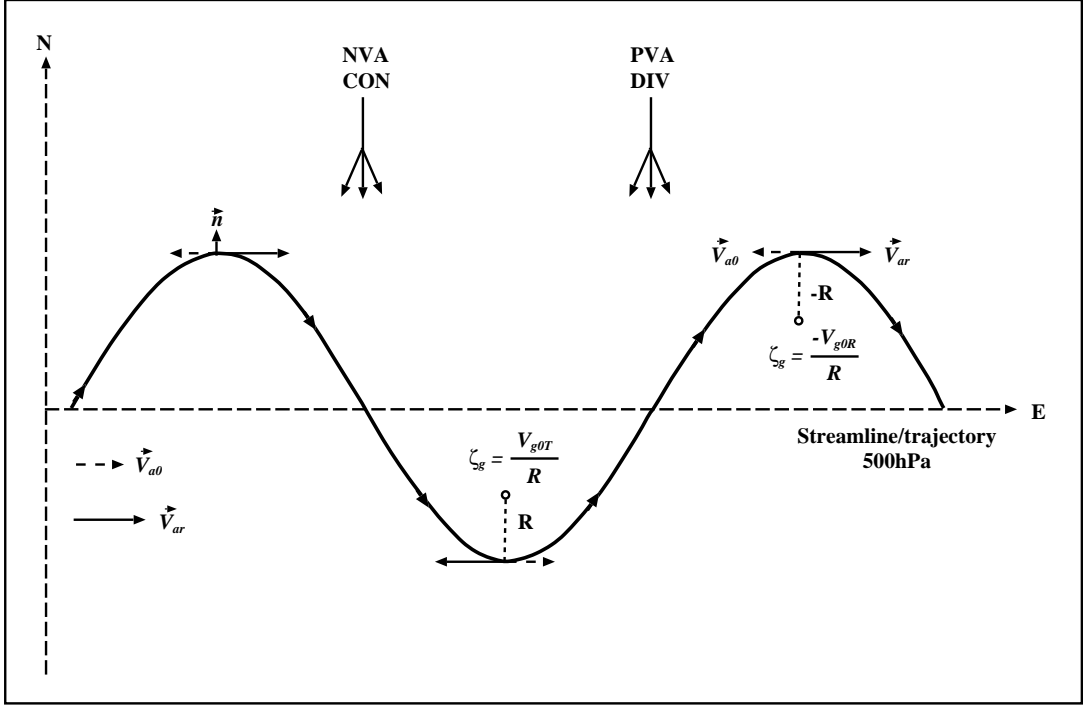


Figure 1: Idealized upper-level wave indicated by a streamline coincident with the axis of the upper-level jet. NVA and PVA are regions of negative and positive relative vorticity advection, respectively. CON and DIV are regions of convergence and divergence, respectively. R is the radius of curvature of the streamline and \vec{n} is the normal unit vector in the natural coordinate system. Thin dashed arrows show \vec{V}_{a0} , the contribution to the ageostrophic wind from the latitudinal variation of the Coriolis parameter f , and full black arrows represents \vec{V}_{ar} , the flow curvature contribution to the ageostrophic wind (see text for more details). Finally, V_{g0T}/R and $-V_{g0R}/R$ is the geostrophic vorticity at the trough and ridge, respectively.

$$\omega \propto \frac{f_0}{\sigma} DVA - \frac{1}{\sigma} TA. \quad (8)$$

Here $VA = -\vec{V}_{g0} \cdot \nabla_p(\zeta_{g0} + f)$ is the absolute geostrophic vorticity advection, $TA = -\vec{V}_g \cdot \nabla_p(RT/p)$ is the geostrophic advection of specific volume $\alpha = (RT/p)$, here interpreted as a pressure weighted temperature advection, $DVA = \frac{\partial}{\partial p} VA$ is the differential vorticity advection and $DTA = \frac{\partial}{\partial p} TA$ is a corresponding pressure weighted differential temperature advection. Note that we have used that $\nabla_p^2(-\vec{V}_{g0} \cdot \nabla_p T) \propto \vec{V}_{g0} \cdot \nabla_p T$ for the second term on the rhs of (6). Note also that $(R/p)\nabla_p T = \nabla_p(RT/p)$, since the gradient is taken at constant pressure.

4. Physical interpretation of the quasigeostrophic equations

4.1. A steady-state zonal wave

Consider first a sinusoidal wave along the west-east direction (i.e. a zonal wave) on a pressure surface in the upper troposphere. The wave is assumed to be in a steady-state, which means that the geopotential field (and hence the geostrophic wind and temperature) does not change with time. In Figure 1 the standing wave is shown by a streamline/trajectory, which also represents a jet axis. Steady-state implies that the secondary circulation must exactly eliminate changes in geostrophic wind and temperature due to advection by the geostrophic wind. It is explained below how this cancellation occurs.

In the QG framework the rate of change of the absolute *geostrophic* vorticity following the *geostrophic* motion is given by (9).

$$\frac{D_g}{Dt}(\zeta_{g0} + f) = -f_0 \nabla_p \cdot \vec{V}_a, \quad (9)$$

Here \vec{V}_a is the ageostrophic wind velocity, $\zeta_{g0} = 1/f_0 \nabla_p^2 \Phi$ is the geostrophic relative vorticity, Φ is the geopotential and $D_g/Dt = \partial/\partial t + u_{g0}\partial/\partial x + v_{g0}\partial/\partial y$ is the rate of change operator following the *geostrophic* motion.

In the natural coordinate system the relative geostrophic vorticity reads

$$\zeta_{g0} = -\frac{\partial V_{g0}}{\partial n} + \frac{V_{g0}}{R}. \quad (10)$$

In (10) R is the radius of curvature, $V_{g0} = (u_{g0}^2 + v_{g0}^2)^{1/2}$ and n is the direction perpendicular and to the left of the flow direction (see Figure 1). At the jet axis, where the geostrophic wind has its maximum, the shear vorticity ($-\partial V_{g0}/\partial n$) is zero, while it is positive (cyclonic) and negative (anticyclonic) on the poleward and equatorward side of the jet axis, respectively.

Air parcels traveling with the geostrophic wind along the jet axis from trough to downstream ridge of the wave in Figure 1 experiences a decrease in ζ_{g0} from V_{g0T}/R (>0) to $-V_{g0R}/R$ (<0) and an increase of planetary vorticity from f_T to f_R . V_{g0T} , f_T and V_{g0R} , f_R are the geostrophic wind speed and Coriolis parameter at the trough and ridge, respectively.

For the relatively short waves involved in rapid cyclogenesis the increase in planetary vorticity is more than compensated by the decrease in ζ_{g0} , implying that $D_g/Dt(\zeta_{g0} + f) < 0$. Then, according to (9), such waves must have a *divergent* flow ($\nabla_p \cdot \vec{V}_a > 0$) between trough and downstream ridge, and a corresponding *convergent* flow ($\nabla_p \cdot \vec{V}_a < 0$) between trough and upstream ridge. The divergent and convergent ageostrophic flow can also be directly visualized by noting that the flow due to the effect of curvature is sub-geostrophic at the trough and super-geostrophic at the ridge. The ageostrophic flow along the jet axis due to latitudinal variations in f (\vec{V}_{a0}) and due to curvature of the flow (\vec{V}_{ar}) is shown schematically in Figure 1 by dashed and full arrows, respectively. Note that the ageostrophic wind is zero at the inflection points, where $|R|$ is infinity (see Appendix for details). Note also that \vec{V}_{a0} for a zonal wave is always *convergent* between trough and downstream ridge. However, for a meridional wave with wind from the north

\vec{V}_{a0} would be divergent between trough and downstream ridge, since f increases with latitude. In contrast \vec{V}_{ar} , the ageostrophic wind due to curvature (defined in Appendix A), is *always* divergent between trough and downstream ridge, regardless of the flow direction and orientation of the wave.

As noted above, in short waves (as in Figure 1) \vec{V}_{ar} is larger than \vec{V}_{a0} . In such waves the total ageostrophic flow \vec{V}_a is therefore divergent/convergent between trough and downstream/upstream ridge.

The vorticity equation (9) can be written in the form

$$\frac{\partial \zeta_{g0}}{\partial t} = -\vec{V}_{g0} \cdot \nabla_p(\zeta_{g0} + f) - f_0 \nabla_p \cdot \vec{V}_a, \quad (11)$$

showing that the rate of change with time of geostrophic vorticity is due to advection of absolute geostrophic vorticity (first rhs term in (11)) and vorticity spin-up or vorticity spin-down by the divergent ageostrophic motion (second rhs term in (11)). In the steady-state case ($\frac{\partial \zeta_{g0}}{\partial t} = 0$) these two terms cancel. Consequently, between trough and downstream ridge the *positive* vorticity advection (PVA) must be eliminated by vorticity spin-down in the *divergent* ageostrophic flow. Similarly, between trough and upstream ridge the *negative* vorticity advection (NVA) must be eliminated by vorticity spin-up in the *convergent* ageostrophic flow. Therefore, in a steady-state wave the ageostrophic motion *completely* cancels advective changes by the geostrophic wind. In a non-steady wave the counteracting secondary circulation is not efficient enough to keep pace with the advective changes by the geostrophic wind. In connection with such waves baroclinic instability may occur.

4.1.1. Sign of vertical velocity

Neither the sign nor the magnitude of the vertical motion in the secondary circulation can be deduced from (11). However, the sign of ω can be deduced from (8). To keep things as simple as possible we assume that TA in (8) is negligible at the considered pressure level. Observations show that TA often is small in the upper troposphere, where isotherms tend to follow the height contours. Interesting exceptions are cases with strongly sloping tropopause. These cases are usually associated with very strong cyclogenesis. With $TA = 0$ the sign of ω is determined by the first term on the rhs of (8). This term is proportional to the differential vorticity advection (*DVA*). If the differential vorticity advection is negative, i.e. if the vorticity advection increases (becomes more cyclonic) with height (considering $f_0/\sigma > 0$), then ω becomes negative, implying upward motion.

4.1.2. Extremes of vorticity advection, divergence and vertical velocity

If $TA = 0$ at the level of maximum VA (where $DVA=0$) both terms on the rhs of (8) are zero, implying that ω must be zero at this level, with upward motions below and downward motions above. The level of *maximum* positive VA and *maximum* negative VA is often found in the upper troposphere. This is a consequence of the prevailing increase with height of the zonal flow in the troposphere. The latter is mainly a result of radiative processes retaining a relatively cold polar troposphere. The approximation

of the lhs of (8) also implies that the level of maximum VA (in absence of TA) tends to be a level of maximum divergence and convergence. This can be seen by taking the derivative with respect to pressure of the continuity equation, yielding

$$\frac{\partial}{\partial p}(\nabla_p \cdot \vec{V}_a) = -\frac{\partial^2 \omega}{\partial p^2} \propto \omega \quad (12)$$

At a level (horizontal) sea or land surface $\omega \approx 0$. Then, according to (12) there must also be a maximum in convergence and divergence at the surface. It can be seen directly from the continuity equation that a level of maximum $|\omega|$ also is a level of no divergence. If there is only one level of no divergence in the troposphere, which tends to be the case in regions of cyclogenesis, a vertical column of air extending from the surface to the jet stream level has a maximum of $|\nabla_p \cdot \vec{V}_a|$ and opposite signs of $\nabla_p \cdot \vec{V}_a$ at the top and bottom of the column.

4.2. Non-amplifying waves

In order to illustrate the isolated effect of VA , the wave in Figure 1 is now considered to be in an equivalent barotropic atmosphere. In such an atmosphere the geostrophic TA is by definition everywhere identical zero, implying that the geostrophic wind does not change direction with height. With cold air poleward of the jet axis in Figure 1 the geostrophic wind speed (according to the thermal wind equation) increases with height. At the jet axis ζ_{g0} is proportional to the geostrophic wind speed (\vec{V}_{g0T}/R and $-\vec{V}_{g0R}/R$ at the trough and ridge, respectively), implying an increase with height of VA . Then, according to (8) there must be *upward* motion between trough and downstream ridge and *downward* motion between trough and upstream ridge. Some researchers refer to the gentle rising motions ahead of upper-level troughs as warm conveyor belts (Browning, 1990). In satellite images the warm conveyor belts usually can be seen as elongated (from quasi-zonal to quasi-meridional) bands of mainly stratiform clouds. Similarly, downward motion between trough and upstream ridge advects dry air from the upper troposphere or lower stratosphere downward and along the jet. By some researchers this dry air stream is called the dry intrusion (Browning, 1990). The dry intrusion is cloud resolving and often forms a sharp cloud edge along the poleward side of the warm conveyor belt clouds.

Due to the steady-state assumption the wave considered here can not amplify. Even a non-steady zonal wave (with neglect of friction and diabatic heating) does not amplify in an equivalent barotropic atmosphere. This follows from (7). At trough and ridge lines VA is zero, because both $\vec{V}_{g0} \cdot \nabla_p \zeta_{g0}$ and $\vec{V}_{g0} \cdot \nabla f$ is zero. This means that the first term ($-f_0 \cdot VA$) on the rhs of (7) is zero, and since $TA = 0$, also the second term is zero. At trough and ridge lines in the considered equivalent barotropic zonal wave the rhs of (7) is therefore zero, which means that $\chi = \partial\phi/\partial t$ also must be zero at trough and ridge lines. In other words, the non-steady wave propagates eastward without amplification, since amplification means that the geopotential height ϕ at the trough and ridge decreases and increases with time, respectively.

4.3. Conditions for wave amplification

Equation (7), term $(f_0^2/\sigma)DTA$ shows that the condition for wave amplification is that TA must increase with height ($DTA < 0$) below the trough and decrease with height ($DTA > 0$) below the ridge.

In the troposphere TA tends to be small at upper levels. In an amplifying wave the typical situation is therefore: Cold advection below the trough ($DTA < 0$) and warm advection below the ridge ($DTA > 0$).

4.4. Low-level thermal advection and diabatic heating

Consider now a west-east oriented (i.e. zonal) frontal zone in the lower troposphere in which there is embedded closed circulations around low and high pressure centers (Figure 2). For simplicity the arguments apply in a reference system moving with the phase velocity of the low-level pressure systems. Further, it is assumed that there is initially a zonal westerly flow aloft without VA and TA . From Figure 2 it is clear that there is cold and warm advection west and east of L, respectively. Because of the vanishing TA aloft both cold and warm advection decreases with height. Then, due to the differential temperature advection (term DTA in (7)), the geopotential height must increase with time above the lower-tropospheric maximum in TA and decrease with time above the lower-tropospheric minimum in TA . Note that the geopotential tendencies have opposite signs below the level of maximum TA . Therefore, below this level the geopotential height (or surface pressure) decreases and increases with time east and west of the surface low, respectively. This creates an eastward propagation of the low-level pressure pattern, which explains the choice of a reference system moving with the low-level system.

In response to the low-level TA a wave system develops aloft with ridge and trough lines above the maximum in warm and cold advection, respectively. The wave lags 45° behind the low-level system, which means that the trough and ridge lines tilt westward (upstream) with height. It has earlier been emphasized that the secondary circulation in a developing system counteracts advective changes by the geostrophic wind. If diabatic processes are neglected, warm and cold advection should therefore be connected with rising and sinking motion leading to adiabatic cooling and warming, respectively. This is consistent with the vertical motion deduced from (8). At the ridge and trough lines of the developing wave aloft the first term (DVA) on the rhs is zero, while the second term ($\sigma^{-1}TA$) is positive for warm advection and negative for cold advection. Therefore ω must be positive (downward motion) in the region with cold advection and negative (upward motion) in the region with warm advection.

In a growing wave it is easy to remember how the secondary circulation responds to advective and diabatic changes. The secondary circulation counteracts these changes. For example is warm advection and diabatic heating associated with rising motion (i.e. with adiabatic cooling due to the secondary circulation). In the same way is cold advection and diabatic cooling associated with sinking motion (i.e. with adiabatic warming due to the secondary circulation). Note how diabatic heating/ cooling associated with phase changes of water tends to counteract the adiabatic cooling/heating effect of the secondary circulation induced by warm/cold advection. Consequently, a stronger sec-

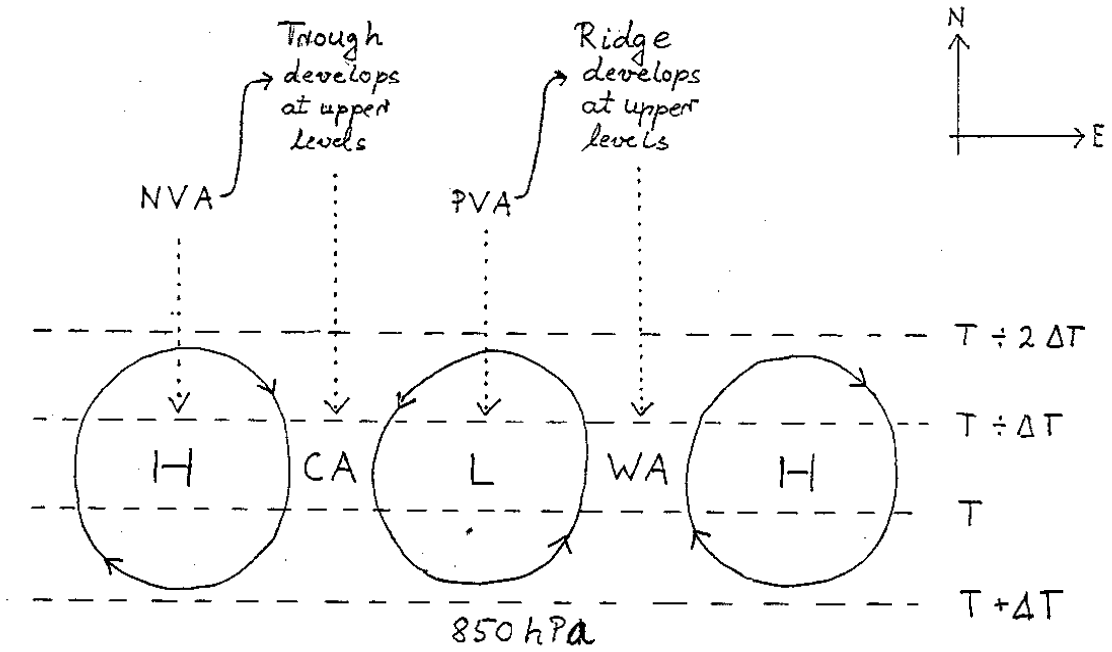


Figure 2: Idealized low-level closed circulations superimposed on a frontal zone. CA and WA are centers of low-level cold and warm advection, respectively. NVA and PVA are negative and positive relative vorticity advection centers, respectively, of the developing wave aloft.

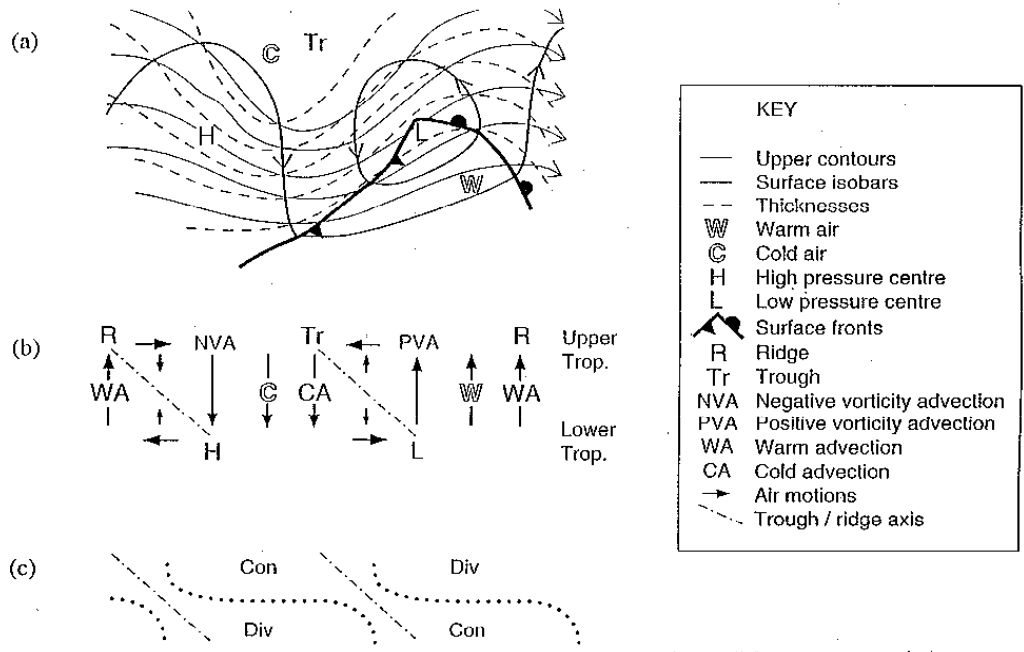


Figure 3: An unstable wave (a) from above, (b) from the side, (c) from the side, showing regions of convergence (Con) and divergence (Div) separated by dotted lines. From Bader et al., 1995.

ondary circulation is needed to eliminate a disturbance generated by geostrophic temperature advection, if the secondary circulation induced by the disturbance is able to trigger phase changes of water.

In the discussion of the steady-state wave in section 4.1 it was shown how geostrophic VA was completely eliminated by the divergent secondary circulation. Similarly, for a steady wave with non-zero temperature advection, adiabatic changes of the temperature by the secondary circulation must eliminate completely the changes due to the geostrophic temperature advection. If phase changes of water occur, the secondary circulation must be stronger to retain a steady state.

5. Baroclinic instability related to upper-tropospheric waves

The discussion in connection with Figure 1 shows that the growing wave aloft, indicated in Figure 2, has positive VA and divergence above L and negative VA and convergence above H (provided that the wave length is not too large). Accordingly, above L and below the level of maximum wave induced VA aloft there must be rising motion, and similarly there must be sinking motion above H . Hence, at the lower-tropospheric level shown in Figure 2 there must be divergence at H and convergence at L . At the low level, where VA is small (isolines of vorticity are approximately parallel to the height contours or surface pressure isobars), the geostrophic vorticity equation (9) simplifies to

$$\frac{\partial \zeta_{g0}}{\partial t} = -f_0 \nabla_p \cdot \vec{V}_a, \quad (13)$$

showing that the secondary circulation associated with the growing wave aloft at low levels gives rise to vorticity spin-up ($\partial \zeta_{g0}/\partial t > 0$) in L and vorticity spin-down ($\partial \zeta_{g0}/\partial t < 0$) in H . We also have $\partial \zeta_{g0}/\partial t = 1/f_0 \nabla_p^2 \partial \phi / \partial t \propto -1/f_0 \partial \phi / \partial t$, implying that the pressure (geopotential height) falls at L and rises at H . The intensification of the low-level system leads to an increase in the low-level wind speed. This enhances TA , which further amplifies the wave aloft, which further increases VA aloft, and which further intensifies the low-level system. The interactions describes a positive feedback between vorticity advection aloft and temperature advection at low level. The interaction occurs through the secondary circulation forced by VA aloft and by TA at low levels. The positive feedback process outlined here describes basically how baroclinic instability works.

The example in Figure 2 has been chosen, because it gives a relatively simple picture of how baroclinic instability works. However, it must be pointed out that it is not typical in the atmosphere that extratropical cyclogenesis is initiated by low-level TA . It is more the rule that the closed circulations in the low-level baroclinic zone in Figure 2 develop in response to upper-level forcing (VA) associated with waves and/or jet streaks, which are the most common precursors of extratropical cyclogenesis. The connection between jet streak dynamics and cyclogenesis is discussed in Section 6. If the troposphere in the region of cyclogenesis has a low static stability the upper-level and low-level forcing may give rise to significant diabatic heating (release of latent heat) in the regions of ascent induced by the forcing. The diabatic heating tends to have its maximum in the lower to middle troposphere. Its effect is similar to low-level warm advection. Numerical studies indicate that it can be a significant forcing term in extratropical cyclogenesis. The latent heat release replaces or supplement low-level warm advection in the positive feed-back between the low-level and upper-level forcing in the cyclogenesis.

It is not always the case that a positive feed-back takes place. If, for example, there is a preexisting wave aloft with a trough above WA and a ridge above CA in Figure 2, then the positive feed-back described above is replaced by a negative feed-back. The latter leads to a damping of both the wave aloft and the closed circulations in the low-level frontal zone.

The shown examples highlight important aspects of baroclinic instability. Firstly, the level of maximum VA must be *vertically* separated from the level of maximum TA /diabatic heating, and secondly, the lines connecting the centers of maximum VA with those of maximum TA /diabatic heating must tilt upstream (westward) with height, i.e. they must be separated *horizontally*. Both aspects are clearly present in Figure 2 and 3. The ‘separation in space’ conditions are necessary, but not sufficient for extratropical cyclogenesis to take place. Both the horizontal and vertical separation must be so small that interaction can take place. The conditions for interaction depend on the static stability and on the scales and relative positions of the perturbations generating the extremes of upper-level VA and low- to mid-level TA /diabatic heating. In the ideal case the penetration depth is of the order $H = f_0 L / N$, where L is the horizontal scale of the perturbation and N (the Brunt-Väisälä frequency, $N^2 = (gp/RT_0)^2 \sigma$), a measure of the static stability of the air (Hoskins et al., 1985). The latter relationship indicates that the efficiency of the baroclinic process depends most critically on the static stability (σ in (5) to (8)) and on the horizontal scale L of the amplifying system. Low static stability and small horizontal scales provide the largest growth rates. The reason is firstly that vorticity forcing (i.e. extremes of VA) associated with upper-level disturbances for a given wind speed and a given wave amplitude tends to be proportional to L^{-3} , and secondly that low static stability (small σ or N) provides the latter disturbances with so large penetration depths that their secondary circulations are able to interact with the low-level flow. Thirdly, the forcing of the secondary circulation (rhs of (8)) and the forcing of wave amplification (second term on the rhs of (7)) is proportional to σ^{-1} . Note for example that for a geopotential field

$$\phi(x, y, t) = \hat{\phi} \sin \frac{2\pi}{L}(x - ct) - f_0 U y + \phi_0, \quad (14)$$

where $\hat{\phi}$ and ϕ_0 are positive constants, U a constant zonal wind and c the phase speed, the relative vorticity advection is

$$-\vec{V}_g \nabla \zeta_g = \frac{(2\pi)^3}{f_0} \frac{U}{L^3} \hat{\phi} \cos \frac{2\pi}{L}(x - ct). \quad (15)$$

For this particular wave, VA is proportional to the upper-level zonal wind. The amplitude $\hat{\phi}$ is generally a function of wave length (short waves tend to have smaller amplitudes than long waves). If the amplitude is proportional to wave length (likely to be an upper-bound estimate) the vorticity advection in (15) is inversely proportional to L^2 .

6. Baroclinic instability related to upper-tropospheric jet streaks

It has been documented that jet streak dynamics plays a significant role in some extratropical cyclone developments (e.g. Uccellini and Kocin, 1987). Therefore, it is also relevant to consider baroclinic instability in relation to upper-tropospheric jet streaks.

For simplicity, it is assumed that the jet streak is linear, implying that the curvature vorticity is zero. Further, it is assumed that its horizontal scale is so small that advection of planetary vorticity can be neglected.

A jet streak is a wind maximum in the core of a jet stream. Typically a jet streak can be identified in the isotac pattern on a pressure surface (in the upper troposphere) as a "lens" shaped structure. Figure 4 shows in schematic form a linear jet streak embedded in a zonal flow. The flow is confluent in the entrance region upstream of the wind maximum and diffluent in the exit region downstream of the wind maximum.

6.1. Entrance and exit regions

In the confluence region the geostrophic wind speed increases downstream (it is assumed that the propagation velocity of the jet streak is slow compared with the speed of the air particles). Air particles that enter the confluence region (the entrance region) of the jet streak are seen to accelerate. According to (19) in the Appendix the acceleration is equal in magnitude and in the opposite direction of the Coriolis force acting on the horizontal ageostrophic wind \vec{V}_{ar} . The acceleration has a maximum on the jet axis and decreases both to the north and south of the axis. It can also be seen from (19) that the acceleration is proportional to \vec{V}_{ar} , the ageostrophic wind speed (with f_0 as constant of proportionality). The latter is perpendicular to the acceleration, which means that the ageostrophic wind is directed from south to north in a zonal jet. Due to the decrease of \vec{V}_{ar} with distance from the jet axis the left entrance of the jet streak is a region of convergence and the right entrance is similarly a region of divergence. If the jet streak is located near the tropopause (which is often the case) it can be assumed that the vertical velocity is zero at the jet streak level (see discussion in section 4.1.2). It then follows from mass continuity that there must be sinking motion below the jet streak in its left entrance region and rising motion below its right entrance region.

In the exit region of the jet streak the air particles desaccelerate, which means that the ageostrophic horizontal wind must be directed from north to south (i.e. in the opposite direction of the ageostrophic wind in the entrance region). Therefore, the exit region has divergence and convergence in its left and right part, respectively. Below the exit region of the jet streak there is rising motion in its left part and sinking motion in its right part.

6.2. Vorticity advection and secondary circulation

The pattern of vertical motion is consistent with the pattern of vorticity and vorticity advection (VA) depicted in Figure 4c. The relative vorticity in a linear jet streak has only contribution from shear vorticity (first term on the rhs of equation (10)). The shear vorticity is zero on the jet axis and positive and negative on the cold and warm side of the axis, respectively. Maximum values of positive and negative shear vorticity occur at the core of the jet streak, since the velocity shear is largest here. Qualitatively, the relative vorticity pattern in a linear jet streak is therefore as depicted in Figure 4c. Since the air particles move through the jet streak from left to right (it is assumed that the jet streak propagation is small compared to the wind speed) the vorticity advection pattern is as depicted in figure 4c with positive VA (PVA in the figure) in the right entrance and

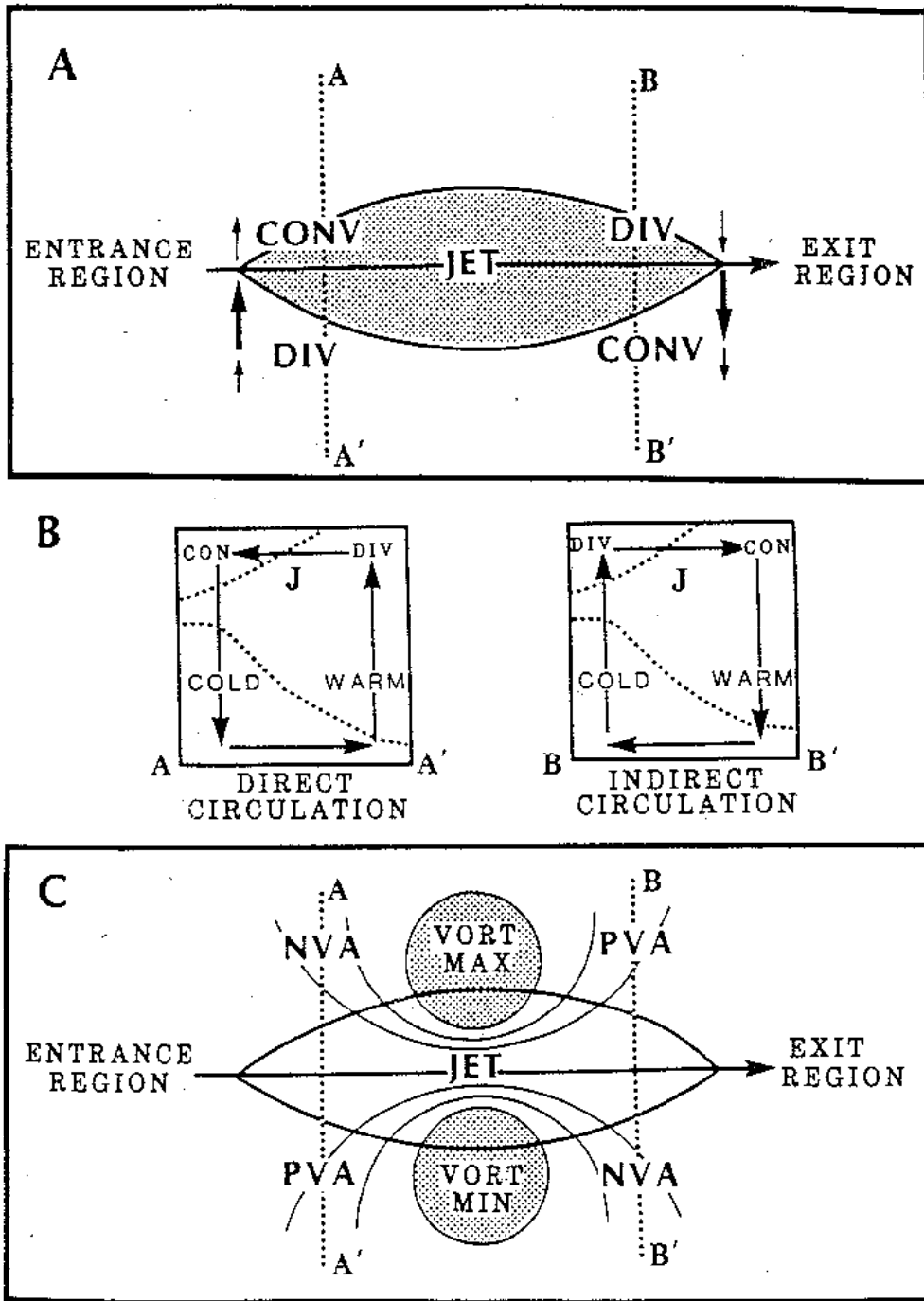


Figure 4: (A) Schematic of transverse ageostrophic wind components and patterns of divergence (DIV) and convergence (CON) in a straight jet streak. (B) Vertical cross sections along AA' and BB' in (A) showing the secondary circulation. J shows the jet axis. (C) Relative vorticity and associated advection patterns in a straight jet streak. After Kocin and Uccellini, 1990.

left exit region, and negative VA (NVA in the figure) in the left entrance and right exit region. At low levels VA is weak. Differential VA therefore becomes more cyclonic with height in the right entrance and left exit region and more anticyclonic with height in the left entrance and right exit region. Then, according to the ω -equation (8), differential VA gives rising motion below the right entrance and left exit region and sinking motion below the left entrance and right exit region, as depicted in Figure 4b. If the surface is level, $\omega \approx 0$ (no flow through the surface). If further diabatic heating and TA is zero at upper levels it follows from (8) that $\omega = 0$ also at the jet streak level (where the absolute VA has its maximum). If there is only one level of no divergence below the entrance and exit regions of the jet streak the secondary circulation becomes as depicted in Figure 4b. The maximum in $|\omega|$ occurs at the level of no divergence. The secondary circulation is thermal direct in the entrance region, since warm air rises and cold air sinks, but thermal indirect in the exit region, since cold air rises and warm air sinks. The secondary circulation acts frontolytical in the entrance region and frontogenetical in the exit region. Note that this mechanism tends to propagate the jet streak downstream.

6.3. Interaction between jet streak and low-level circulation

If a low-level closed cyclonic circulation is present below the jet axis in the exit region of an upper-level jet streak there will be low-level warm and cold advection downstream and upstream of the exit. If $TA = 0$ in the jet streak, it follows from (7) that an upper-level wave develops with a ridge and trough downstream and upstream of the exit, respectively. Above the low-level circulation the wave development aloft adds positive VA to the VA of the jet streak, leading to an intensification of the low-level circulation. The secondary circulation in the exit of the jet streak tends to propagate the low-level circulation poleward. The developing wave aloft tends to slow down this propagation. If a low-level closed cyclonic circulation instead is present below the jet axis in the entrance region of a jet streak the secondary circulation of the latter tends to propagate the closed circulation equatorward, while the developing wave aloft tends to slow down the propagation. The degree of interaction between low and upper levels depends on the static stability. In the entrance and exit region the static stability is affected by the secondary circulation associated with the jet streak. In the entrance region ageostrophic TA stabilizes the troposphere (warm advection aloft and low-level cold advection), whereas it destabilizes the troposphere in the exit region (cold advection aloft and low-level warm advection). This mechanism tends to speed up cyclogenesis in the exit region and slow down cyclogenesis in the entrance region, since the forcing terms in (7) and (8) (except VA in (7)) are proportional to σ^{-1} . In addition, there is often a deeper layer of cold air in the left exit than in the right entrance of a jet streak, because the jet streak is embedded in the upper-level jet above the sloping frontal zone. This usually also contributes to a lower bulk static stability in the left exit, since the lapse rate in cold air with a long history over a relatively warmer sea has been modified by convection to become nearly moist adiabatic. Therefore, static stability tends to favor deep surface cyclones below the left exit region in linear upper-level jet streaks.

continues on page 20

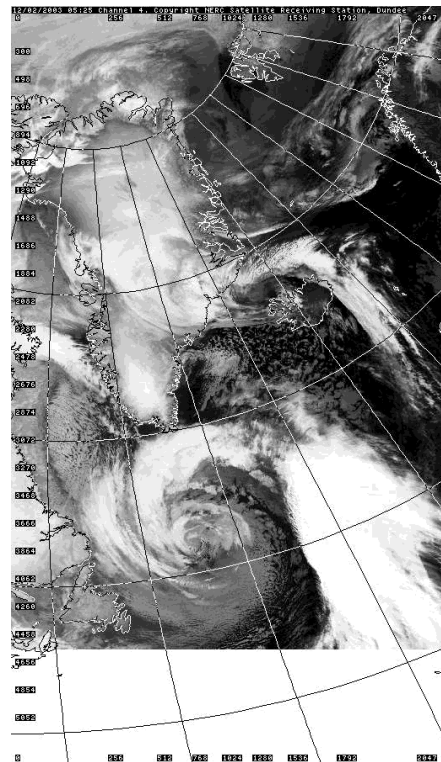
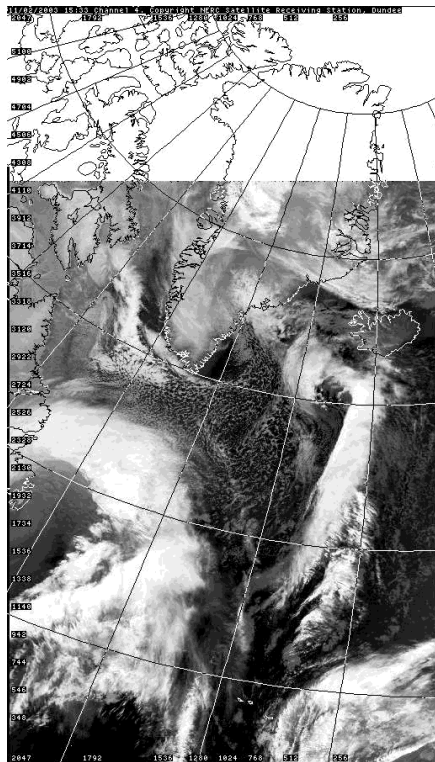
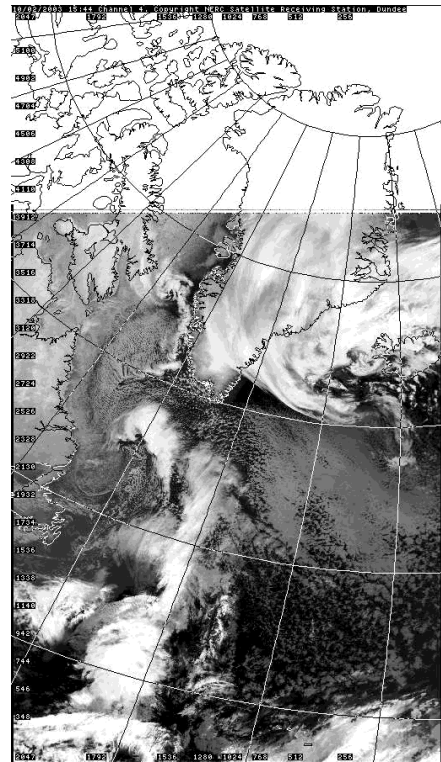
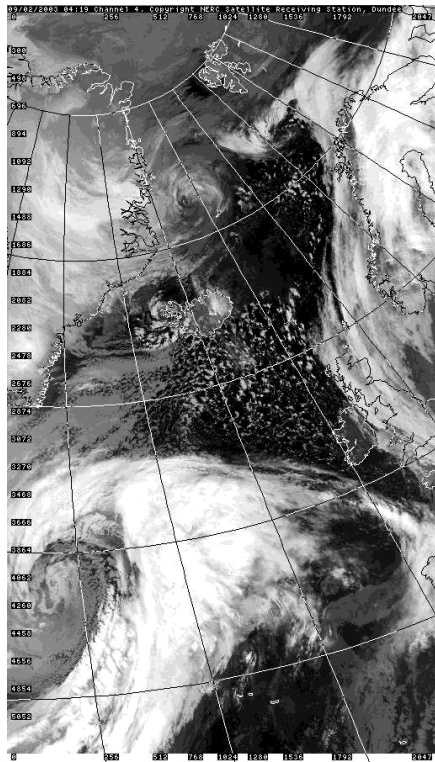


Figure 5: NOAA infrared satellite images. Upper left: 04:19 UTC February 9, upper right: 15:44 UTC February 10, lower left: 15:33 UTC February 11 and lower right: 05:25 UTC February 12. The year is 2003.

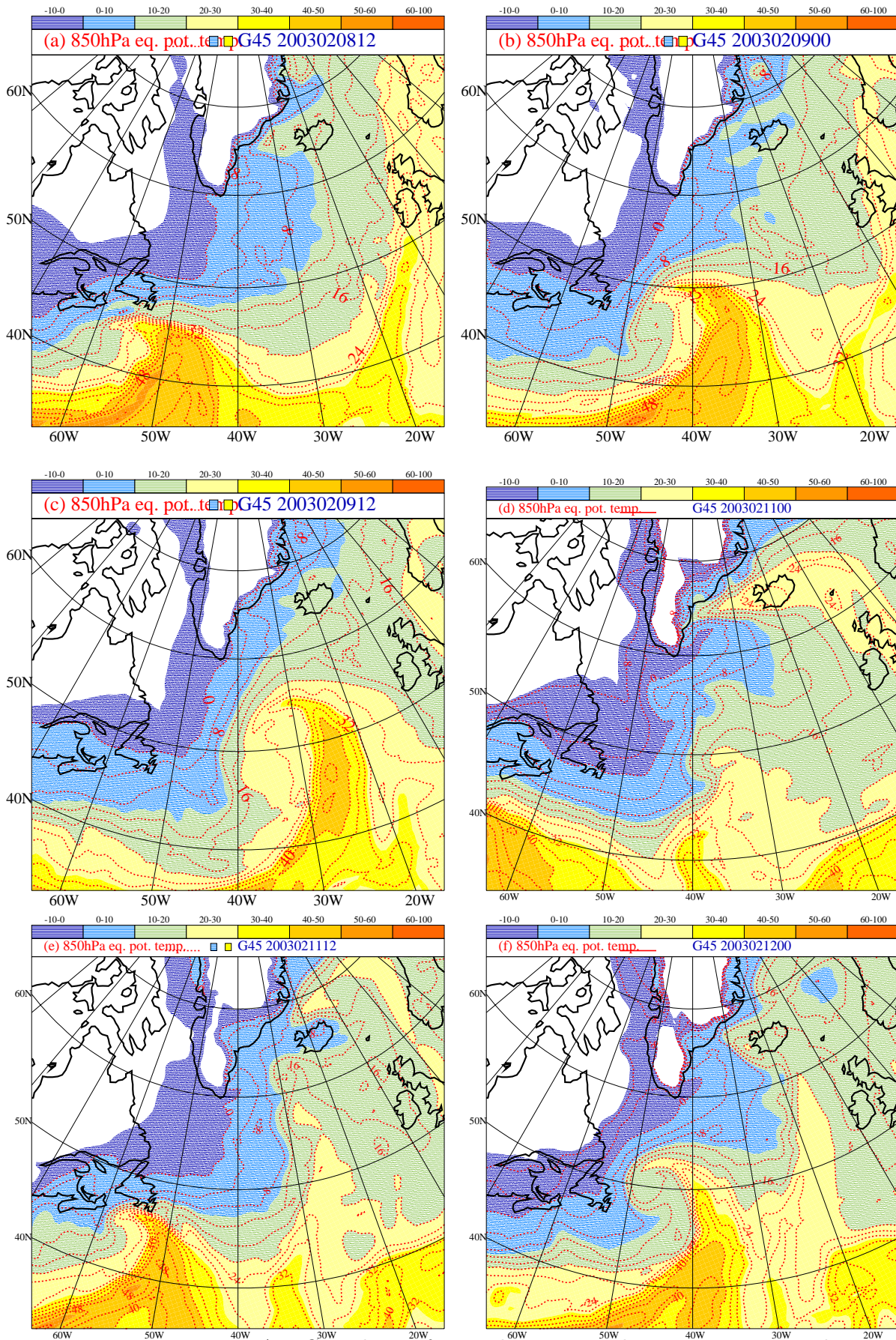


Figure 6: DMI-HIRLAM-G analyses of equivalent potential temperature at 850 hPa at 12 hour intervals in period 1 from 12 UTC February 8 to 12 UTC February 9 and in period 2 from 00 UTC February 11 to 00 UTC February 12. Contour interval is 2 K.

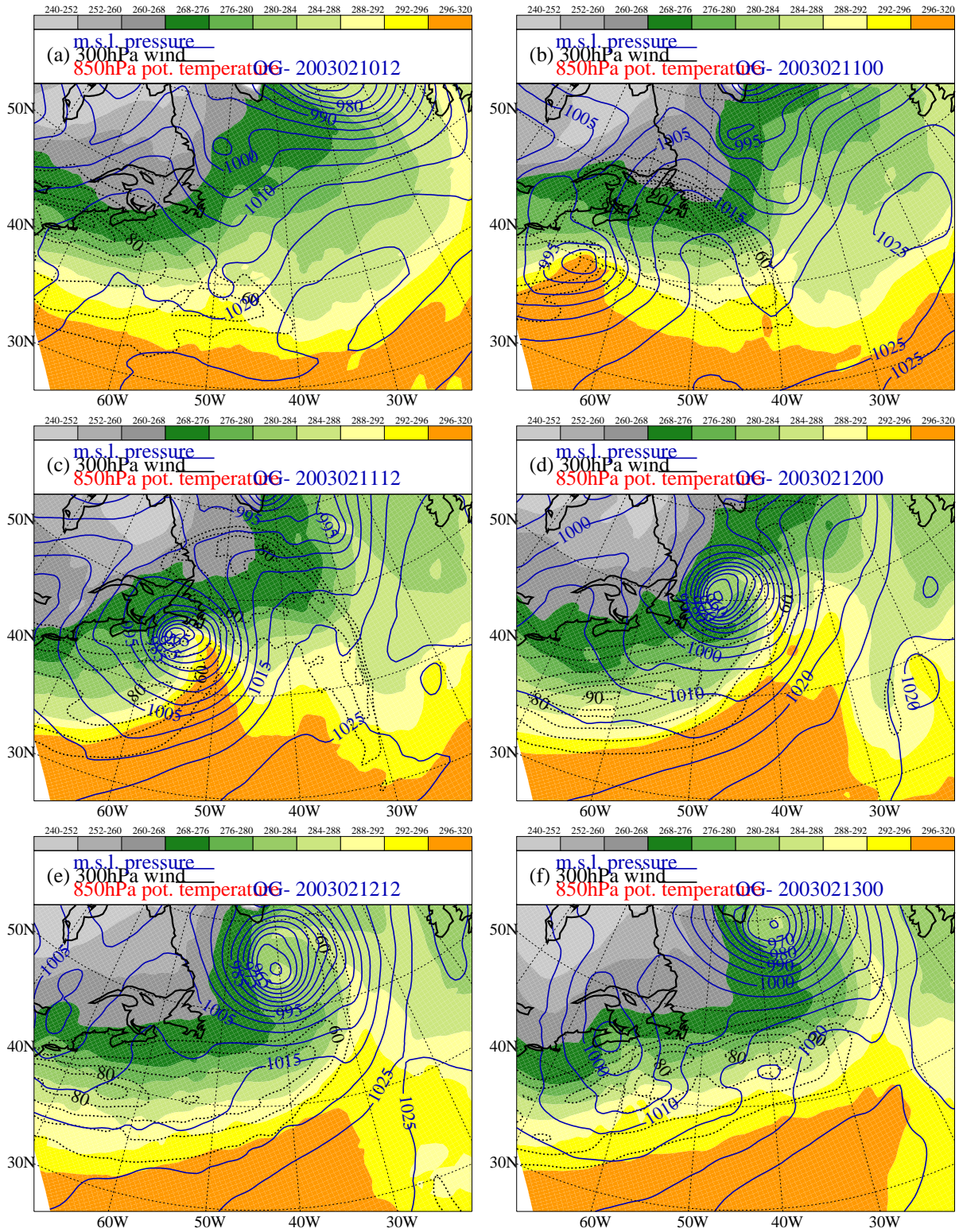


Figure 7: DMI-HIRLAM-G analyses of mslp (full blue curves at 5 hPa intervals), potential temperature at 850 hPa (intervals with different coloring) and wind speed at 300 hPa (black dotted curves at 10 m s^{-1} intervals. Minimum contour drawn is 50 m s^{-1}). Analyses are shown at 12 hour intervals from 12 UTC February 10 to 00 UTC February 13.

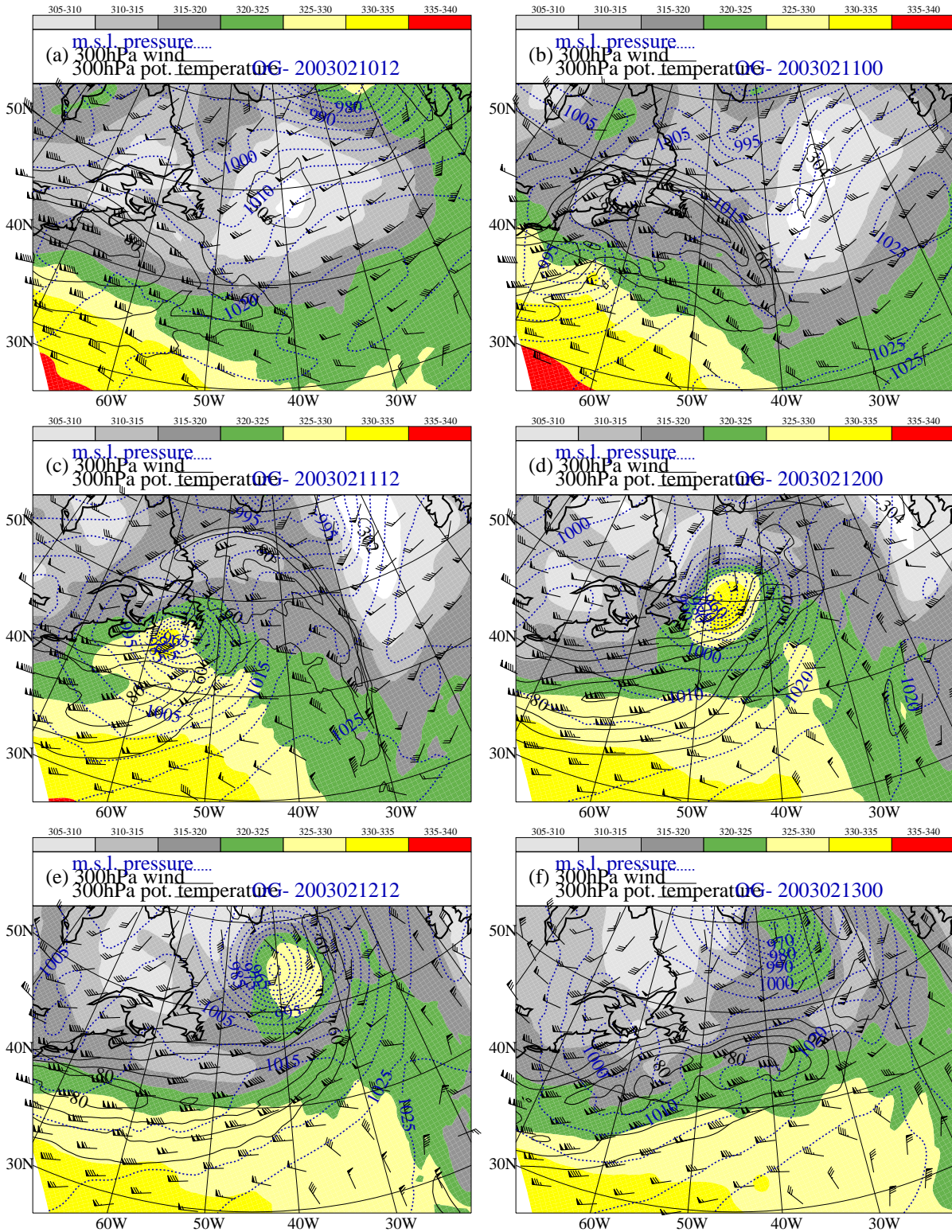


Figure 8: DMI-HIRLAM-G analyses of mslp (dotted blue curves at 5 hPa intervals), potential temperature at 300 hPa (intervals with different coloring), wind speed at 300 hPa (full black curves at 10 m s⁻¹ intervals. Minimum contour drawn is 50 m s⁻¹) and wind velocity (WMO standard) at 300 hPa. Analyses are shown at 12 hour intervals from 12 UTC February 10 to 00 UTC February 13.

If further a jet streak is superposed on an upper-level short-wave trough deepening of surface cyclones tends to be enhanced and suppressed in the left exit and right entrance region, respectively. Note that this change in deepening of the surface cyclone is expected, since upper-level vorticity advection from wave and jet streak dynamics has the same and opposite signs in the left exit and right entrance region, respectively. If, on the other hand, a jet streak is superposed on an upper-level ridge a weakening and strengthening of surface cyclones occurs in the left exit and right entrance region, respectively.

7. Examples of extratropical cyclogenesis

Figures 5 to 8 show examples of cyclogenesis over the North Atlantic east of Newfoundland. The period considered is from 12 UTC February 8 to 00 UTC February 13 in 2003. Within this short period (4.5 days) two intense cyclones developed. In addition a polar low (or comma cloud) developed in the the short period between the two intense cyclogenesis events. Figure 5, upper left, shows the first cyclone in its most intense (mature) phase. Figure 5, upper right, shows a fully developed polar low over the Labrador Sea, south-southwest of the southern tip of Greenland. Note the much smaller horizontal scale of the polar low. Figure 5, lower left, shows the second intense low (in the lower left quadrant), approaching its mature stage. The polar low can still be identified at a position southwest of Island. Finally, Figure 5, lower right, shows the second deep low in its dissipating stage south of Greenland. The two deep lows as well as the polar low can also be identified in Figure 6. This figure shows how θ_e , the equivalent potential temperature, changes with time at 850 hPa in the region of cyclogenesis. Figures 6a to 6c show the development of the θ_e pattern at 850 hPa associated with the first intense low. The low-level thermal structure appears to be in agreement with the conceptual model of Shapiro and Keyser, 1990. In the rapid deepening phase of the cyclone, it has formed a bent-back front and a frontal fracture (Figure 6a). The frontal fracture refers to a considerable weakening of the cold front in the region, where it merges with the warm front. As the development proceeds, the bent-back front begins to encircle the surface low. At the stage of development shown by Figure 6b the low-level fronts form a T-bone structure with a clear frontal fracture and a cold front that is nearly perpendicular to the warm front. In the mature to dissipating stage the cyclone has formed a warm core seclusion, i.e. with an isolated region of relatively warm and moist air at the center of the low. The analysis in Figure 6c shows the mature stage of the cyclone, but a clear warm core seclusion can not be identified. However, a warm core seclusion can be identified in the mature to dissipating stage of the second intense cyclone (Figure 6e). In Figure 6d the signature of the polar low can be seen south of Greenland at 55°N. In Figure 5, upper right, Figure 6d and Figure 7b there is indication of a second circulation center further south at 49°N. Note that the two rapid deepening cyclones form in the same region (Figure 6a and 6e). Formation of successive cyclones in the same region is not uncommon for upstream developments (Shapiro et al., 1999), but as noted previously, the deep cyclones investigated here did not follow in succession.

Figure 7 and 8 show more details about the evolution of the polar low and the second intense cyclone. The evolution of the first deep low is not shown since it is similar to the evolution of the second low. The polar low developed in the period between the

evolution of the first and second intense low. According to Figure 7a and b it had a closed surface circulation and the largest horizontal pressure gradients in its southwest quadrant. Figures 8a and 8b indicate that the polar low developed downstream of an eastward moving upper-level trough. Figure 5, upper right, shows that a complex of clouds was present in the region of ascent downstream of the upper-level trough. This complex contained the second circulation center.

The early stage of the second low is not shown, since the incipient cyclone was outside the model domain of DMI-HIRLAM-G. However, Figures 7a and 8a indicate that the surface low in its incipient stage was located equatorward of the upper-level jet axis. During the period of development it propagated beneath the jet core (Figures 7a and 8a) to its poleward side (Figures 7c and 8c). The upper-level wave associated with the surface cyclogenesis amplified as a result of the positive feed-back between vorticity advection aloft and combined warm advection and diabatic heating at lower levels. Figures 7b to 7d show the rapid deepening period of the cyclone. In this period the surface cyclone propagated beneath the jet core to the left exit region of a jet streak. The exit region was located downstream of the trough of the amplifying wave aloft. In the dissipation stage of the cyclone a closed circulation with an approximately vertical axis of rotation had formed throughout the depth of the troposphere (Figures 7e,f and 8e,f).

Note that at the end of the considered period rather weak surface cyclogenesis took place poleward of the upper-level jet axis downstream of a large-amplitude upper-level trough over Labrador (Figures 7f and 8f). Unlike the rapid deepening cyclones the slowly deepening surface low did not cross beneath the upper-level jet stream during its development.

The θ pattern at 300 hPa (Figure 8) shows that a local maximum developed right above the center of the surface cyclone in its most intense phase (Figure 8d). Such a local maximum of θ in the lower stratosphere is a signature of rapid cyclogenesis. The local maximum first appears upstream (at jet stream level) of the developing surface cyclone and becomes nearly vertically collocated with the surface cyclone in the mature phase of the latter. The local maximum of θ in the lower stratosphere in a region of rapid extratropical cyclogenesis is strongly correlated with the dark region seen on satellite water vapor channel images. A dark region shows the presence of dry air above mid- to upper-tropospheric levels. In rapid cyclogenesis the dark region is typically located at the poleward edge of the warm conveyor belt clouds. Downstream it forms a wedge between the warm conveyor belt clouds and the cloud head of the rapid deepening cyclone (Browning, 1990). In terms of potential vorticity the local θ maximum in the lower stratosphere is a manifestation of a positive potential vorticity anomaly, located at a downward bulge of the tropopause (Hoskins et al., 1985). In more conventional terms the local θ maximum at 300 hPa shows the warm core character of the lower-stratospheric part of the mature cyclone. Note that a mature cyclone in thermal wind balance with an approximately vertical axis of rotation must have a warm core in the lower stratosphere, since the intensity of the circulation decreases with height above the tropopause.

8. Discussion and conclusions

Extratropical cyclogenesis has been interpreted physically by using qualitative arguments based on the quasigeostrophic equations. The arguments have been applied to a five-day sequence of extratropical cyclone developments over the western North Atlantic. The sequence shows cyclogenesis on widely different horizontal scales and on shorter and longer time scales. It gives an impression of the complexity of extratropical cyclogenesis in the atmosphere unmatched by the relative simplicity of idealized models applied in theoretical studies of extratropical cyclogenesis.

Basically, baroclinic instability is a positive feedback between upper-tropospheric vorticity advection and low- to mid-level thermal advection/diabatic heating. The feedback occurs via the secondary circulations connected with differential vorticity advection and temperature advection/diabatic heating. In regions of cyclogenesis the vorticity advection usually is small at low levels, whereas the temperature advection and diabatic heating tends to be weak at upper levels.

In extratropical cyclogenesis the developing secondary circulation associated with TA /diabatic heating feeds positively back on the upper-level secondary circulation by amplifying the upper-level wave and hence increasing VA aloft. It is important to note that if the secondary circulation generates phase changes of water it tends to be intensified, i.e. the efficiency of the positive feed-back tends to be enhanced. The latter feedback is not possible if extremes of VA and TA /diabatic heating are not vertically separated. A positive feedback further requires that lines connecting extremes of VA and TA /diabatic heating of equal sign tilt upstream with height.

In general vorticity advection associated with both upper-tropospheric waves and jet streaks plays a role in extratropical cyclogenesis, but their relative contribution to the cyclogenesis vary from case to case, depending on the structure of the larger-scale flow in which the cyclones evolve.

The preferred regions of extratropical surface cyclogenesis are usually downstream of upper-level troughs. If only a weak amplitude wave is present aloft in the incipient stage of surface cyclogenesis, jet streak dynamics may play an important role right from the start of cyclogenesis. Observations indicate that very rapid deepening cyclones (with horizontal scales of 1000 km or less and time scales of 1 to 2 days) form equatorward of the upper-level jet. During the intensification of the surface cyclone it propagates below the upper-level jet axis to its poleward side. In the mature phase of the surface cyclone it is located below the left exit of a jet streak in the upper-level jet stream. An example of this type of cyclogenesis is presented in Nielsen and Saas, 2003. In cases with a large amplitude wave aloft the incipient low tends to form closer to the jet axis downstream of the upper-level trough. In both cases the maximum deepening rate of the surface cyclone tends to occur as it propagates beneath the upper-level jet core to its cyclonic shear side. During the cyclogenesis the upper-level jet undergoes large changes (both in strength and appearance on an upper-level pressure surface (e.g. 300 hPa)). In some cyclogenesis events the mature surface cyclone is located below a region of overlap between two jet streaks, in the left exit region of a jet streak upstream of the surface cyclone and in the right entrance region of a jet streak downstream of the surface cyclone. However, this configuration appears to be a result of the baroclinic development, not the cause of it. Occasionally, slowly deepening surface cyclones downstream of large-amplitude

upper-level troughs remain poleward of the upper-level jet axis throughout their life cycles.

In recent years several papers, beginning with Hoskins et al., 1985, have applied potential vorticity arguments to explain extratropical cyclogenesis. The potential vorticity arguments are not restricted to the quasigeostrophic system. Nevertheless, in many respects they appear to be similar to the quasigeostrophic arguments used in the present report.

Appendix A.

The frictionless quasigeostrophic momentum equation takes the form

$$\frac{D_g \vec{V}_{g0}}{Dt} = -f_0 \vec{k} \times \vec{V}_a - \beta y \vec{k} \times \vec{V}_{g0}. \quad (16)$$

In (16) the geostrophic wind \vec{V}_{g0} is defined by using a constant Coriolis parameter f_0 , \vec{V}_a is the ageostrophic wind, $\beta = \partial f / \partial y$ and y is the meridional distance from latitude ϕ_0 (being positive and negative north and south of ϕ_0 , respectively).

Consider a steady-state, uniform geostrophic wind field $\vec{V}_{g0} = 1/f_0 \cdot \vec{k} \times \nabla_p \phi$. For such a field the lhs of (16) is zero, implying

$$\vec{V}_a = -\frac{\beta y}{f_0} \vec{V}_{g0}. \quad (17)$$

We also have

$$\vec{V}_g = \frac{1}{f} \vec{k} \times \nabla_p \phi \approx \frac{1}{f_0} \vec{k} \times \nabla_p \phi \cdot \left(1 - \frac{\beta y}{f_0}\right) = \vec{V}_{g0} - \frac{\beta y}{f_0} \vec{V}_{g0} = \vec{V}_{g0} + \vec{V}_{a0}, \quad (18)$$

showing that $\vec{V}_{a0} = -(\beta y / f_0) \vec{V}_{g0}$ is the adjustment to the "constant f " geostrophic wind at other latitudes than f_0 necessary to keep the wind field in geostrophic balance. The latter adjustment, which is necessary because of the latitudinal variation of f , does not involve acceleration of \vec{V}_{g0} . Hence, if we write \vec{V}_a as $\vec{V}_a = \vec{V}_{ar} + \vec{V}_{a0}$ substitution in (16) yields

$$\frac{D_g \vec{V}_{g0}}{Dt} = -f_0 \vec{k} \times \vec{V}_{ar}. \quad (19)$$

It follows from (19) that acceleration of the geostrophic wind \vec{V}_{g0} is equal in magnitude and in the opposite direction of the Coriolis force acting on the ageostrophic wind \vec{V}_{ar} . Equation (19) shows that acceleration in the direction of the geostrophic wind is associated with an ageostrophic wind perpendicular to that direction, while acceleration perpendicular to the direction of the geostrophic wind is associated with an ageostrophic wind in the direction of the geostrophic wind.

In short waves centripetal forces (which are perpendicular to \vec{V}_{g0}) usually dominate, while the acceleration along the direction of \vec{V}_{g0} tends to dominate in jet streaks. Accordingly, in short waves the ageostrophic flow tends to be along the streamlines/trajectories of the geostrophic wind, while it tends to be perpendicular to the geostrophic streamlines/trajectories in linear jet streaks. It can also be noted that (17) shows that \vec{V}_{a0} is in the direction of \vec{V}_{g0} south of latitude ϕ_0 and in the opposite direction north of ϕ_0 .

References

- Bader, M. J., G. S. Forbes, J. R. Grant, R. B. E. Lilley and A. J. Waters (1995). Images in Weather forecasting: A practical guide for interpreting satellite and radar imagery. *Cambridge University Press*, 499 pp.
- Bluestein, H.B. (1992). Synoptic-Dynamic Meteorology in Midlatitudes. Vol. 1. *Oxford University Press*, 431 pp.
- Browning, K. (1990). Organization of clouds and precipitation in extratropical cyclones. In *Extratropical Cyclones: The Eric Palmén memorial Volume*, C.W. Newton and E.O. Holopainen , Eds. , *Amer. Meteor. Soc.*, pages 129–153.
- Charney, J. G.(1947). The dynamics of long waves in a baroclinic westerly current. *J. Meteor.*, 4, 125–162
- Holton, R. J. (1992). An Introduction to Dynamic Meteorology. *Academic Press Inc.*, 507 pp.
- Hoskins, B. J., McIntyre, M. E., and A. W. Robertson (1985). On the use and significance of isentropic potential vorticity maps. *Quart. J. Roy. Meteor. Soc.*, 111, 877–946.
- Kocin, P. J. and L. W. Uccellini (1990). Snowstorms Along the Northeastern Coast of the United States: 1955 to 1985. *Meteor. Monogr.*, 22, No. 44, 280 pp.
- Nielsen, N. W., and B. H. Sass (2003). A numerical, high-resolution study of the life cycle of the severe storm over Denmark on 3 December 1999. *Tellus*, 55A, 338–351.
- Shapiro, M. A. and D. Keyser (1990). Fronts, jet streams and the tropopause. *Extratropical Cyclones: The Eric Palmén memorial Volume*, C.W. Newton and E.O. Holopainin , Eds. , *Amer. Meteor. Soc.*, 167–191.
- Shapiro, M. A., Wernli, H., Bao, J-W., Methven, J., Zou, X., Doyle, J. Holt, T., Donall-Grell, E., and P. Neiman (1999). A Planetary-scale to Mesoscale Perspective of the Life Cycles of Extratropical Cyclones: The Bridge between Theory and Observations. *The Life Cycles of Extratropical Cyclones*, M. Shapiro and S. Grønås , Eds. , *Amer. Meteor. Soc.*, 139–185
- Uccellini, L. W., and P. J. Kocin (1987). The interaction of jet streak circulations during heavy snow events along the East Coast of the United States. *Wea. Forecasting*, 2, 289–308.

DANISH METEOROLOGICAL INSTITUTE

Scientific Reports

Scientific reports from the Danish Meteorological Institute cover a variety of geophysical fields, i.e. meteorology (including climatology), oceanography, subjects on air and sea pollution, geomagnetism, solar-terrestrial physics, and physics of the middle and upper atmosphere.

Reports in the series within the last five years:

No. 99-1

Henrik Feddersen: Project on prediction of climate variations on seasonal to interannual timescales (PROVOST) EU contract ENVA4-CT95-0109: DMI contribution to the final report: Statistical analysis and post-processing of uncoupled PROVOST simulations

No. 99-2

Wilhelm May: A time-slice experiment with the ECHAM4 A-GCM at high resolution: the experimental design and the assessment of climate change as compared to a greenhouse gas experiment with ECHAM4/OPYC at low resolution

No. 99-3

Niels Larsen et al.: European stratospheric monitoring stations in the Arctic II: CEC Environment and Climate Programme Contract ENV4-CT95-0136. DMI Contributions to the project

No. 99-4

Alexander Baklanov: Parameterisation of the deposition processes and radioactive decay: a review and some preliminary results with the DERMA model

No. 99-5

Mette Dahl Mortensen: Non-linear high resolution inversion of radio occultation data

No. 99-6

Stig Syndergaard: Retrieval analysis and methodologies in atmospheric limb sounding using the GNSS radio occultation technique

No. 99-7

Jun She, Jacob Woge Nielsen: Operational wave forecasts over the Baltic and North Sea

No. 99-8

Henrik Feddersen: Monthly temperature forecasts for Denmark - statistical or dynamical?

No. 99-9

P. Thejll, K. Lassen: Solar forcing of the Northern hemisphere air temperature: new data

No. 99-10

Torben Stockflet Jørgensen, Aksel Walløe Hansen: Comment on "Variation of cosmic ray flux and global coverage - a missing link in solar-climate relationships" by Henrik Svensmark and Eigil Friis-Christensen

No. 99-11

Mette Dahl Meincke: Inversion methods for atmospheric profiling with GPS occultations

No. 99-12

Hans-Henrik Benzon; Laust Olsen; Per Høeg: Simulations of current density measurements with a Faraday Current Meter and a magnetometer

No. 00-01

Per Høeg; G. Leppelmeier: ACE - Atmosphere Climate Experiment

No. 00-02

Per Høeg: FACE-IT: Field-Aligned Current Experiment in the Ionosphere and Thermosphere

No. 00-03

Allan Gross: Surface ozone and tropospheric chemistry with applications to regional air quality modeling. PhD thesis

No. 00-04

Henrik Vedel: Conversion of WGS84 geometric heights to NWP model HIRLAM geopotential heights

No. 00-05

Jérôme Chenevez: Advection experiments with DMI-Hirlam-Tracer

No. 00-06

Niels Larsen: Polar stratospheric clouds micro-physical and optical models

No. 00-07

Alix Rasmussen: "Uncertainty of meteorological parameters from DMI-HIRLAM"

No. 00-08

A.L. Morozova: Solar activity and Earth's weather. Effect of the forced atmospheric transparency changes on the troposphere temperature profile studied with atmospheric models

No. 00-09

Niels Larsen, Bjørn M. Knudsen, Michael Gauss, Giovanni Pitari: Effects from high-speed civil traffic aircraft emissions on polar stratospheric clouds

No. 00-10

Søren Andersen: Evaluation of SSM/I sea ice algorithms for use in the SAF on ocean and sea ice, July 2000

No. 00-11

Claus Petersen, Niels Woetmann Nielsen: Diagnosis of visibility in DMI-HIRLAM

No. 00-12

Erik Buch: A monograph on the physical oceanography of the Greenland waters

No. 00-13

M. Steffensen: Stability indices as indicators of lightning and thunder

No. 00-14

Bjarne Amstrup, Kristian S. Mogensen, Xiang-Yu Huang: Use of GPS observations in an optimum interpolation based data assimilation system

No. 00-15

Mads Hvid Nielsen: Dynamisk beskrivelse og hydrografisk klassifikation af den jyske kyststrøm

No. 00-16

Kristian S. Mogensen, Jess U. Jørgensen, Bjarne Amstrup, Xiaohua Yang and Xiang-Yu Huang: Towards an operational implementation of HIRLAM 3D-VAR at DMI

No. 00-17

Sattler, Kai; Huang, Xiang-Yu: Structure function characteristics for 2 meter temperature and relative humidity in different horizontal resolutions

No. 00-18

Niels Larsen, Ib Steen Mikkelsen, Bjørn M. Knudsen m.fl.: In-situ analysis of aerosols and gases in the polar stratosphere. A contribution to THESEO. Environment and climate research programme. Contract no. ENV4-CT97-0523. Final report

No. 00-19

Amstrup, Bjarne: EUCOS observing system experiments with the DMI HIRLAM optimum interpolation analysis and forecasting system

No. 01-01

V.O. Papitashvili, L.I. Gromova, V.A. Popov and O. Rasmussen: Northern polar cap magnetic activity index PCN: Effective area, universal time, seasonal, and solar cycle variations

No. 01-02

M.E. Gorbunov: Radiographic methods for processing radio occultation data in multipath regions

No. 01-03

Niels Woetmann Nielsen; Claus Petersen: Calculation of wind gusts in DMI-HIRLAM

No. 01-04

Vladimir Penenko; Alexander Baklanov: Methods of sensitivity theory and inverse modeling for estimation of source parameter and risk/vulnerability areas

No. 01-05

Sergej Zilitinkevich; Alexander Baklanov; Jutta Rost; Ann-Sofi Smedman, Vasilij Lykosov and Pierluigi Calanca: Diagnostic and prognostic equations for the depth of the stably stratified Ekman boundary layer

No. 01-06

Bjarne Amstrup: Impact of ATOVS AMSU-A radiance data in the DMI-HIRLAM 3D-Var analysis and forecasting system

No. 01-07

Sergej Zilitinkevich; Alexander Baklanov: Calculation of the height of stable boundary layers in operational models

No. 01-08

Vibeke Huess: Sea level variations in the North Sea – from tide gauges, altimetry and modelling

No. 01-09

Alexander Baklanov and Alexander Mahura: Atmospheric transport pathways, vulnerability and possible accidental consequences from nuclear risk sites: methodology for probabilistic atmospheric studies

No. 02-01

Bent Hansen Sass and Claus Petersen: Short range atmospheric forecasts using a nudging procedure to combine analyses of cloud and precipitation with a numerical forecast model

No. 02-02

Erik Buch: Present oceanographic conditions in Greenland waters

No. 02-03

Bjørn M. Knudsen, Signe B. Andersen and Allan Gross: Contribution of the Danish Meteorological Institute to the final report of SAMMOA. CEC contract EVK2-1999-00315: Spring-to.-autumn measurements and modelling of ozone and active species

No. 02-04

Nicolai Kliem: Numerical ocean and sea ice modelling: the area around Cape Farewell (Ph.D. thesis)

No. 02-05

Niels Woetmann Nielsen: The structure and dynamics of the atmospheric boundary layer

No. 02-06

Arne Skov Jensen, Hans-Henrik Benzon and Martin S. Lohmann: A new high resolution method for processing radio occultation data

No. 02-07

Per Høeg and Gottfried Kirchengast: ACE+: Atmosphere and Climate Explorer

No. 02-08

Rashpal Gill: SAR surface cover classification using distribution matching

No. 02-09

Kai Sattler, Jun She, Bent Hansen Sass, Leif Laursen, Lars Landberg, Morten Nielsen og Henning S. Christensen: Enhanced description of the wind climate in Denmark for determination of wind resources: final report for 1363/00-0020: Supported by the Danish Energy Authority

No. 02-10

Michael E. Gorbunov and Kent B. Lauritsen: Canonical transform methods for radio occultation data

No. 02-11

Kent B. Lauritsen and Martin S. Lohmann: Unfolding of radio occultation multipath behavior using phase models

No. 02-12

Rashpal Gill: SAR ice classification using fuzzy screening method

No. 02-13

Kai Sattler: Precipitation hindcasts of historical flood events

No. 02-14

Tina Christensen: Energetic electron precipitation studied by atmospheric x-rays

No. 02-15

Alexander Mahura and Alexander Baklanov: Probabilistic analysis of atmospheric transport patterns from nuclear risk sites in Euro-Arctic Region

No. 02-16

A. Baklanov, A. Mahura, J.H. Sørensen, O. Rigina, R. Bergman: Methodology for risk analysis based on atmospheric dispersion modelling from nuclear risk sites

No. 02-17

A. Mahura, A. Baklanov, J.H. Sørensen, F. Parker, F. Novikov K. Brown, K. Compton: Probabilistic analysis of atmospheric transport and deposition patterns from nuclear risk sites in russian far east

No. 03-01

Hans-Henrik Benzon, Alan Steen Nielsen, Laust Olsen: An atmospheric wave optics propagator, theory and applications

No. 03-02

A.S. Jensen, M.S. Lohmann, H.-H. Benzon and A.S. Nielsen: Geometrical optics phase matching of radio occultation signals

No. 03-03

Bjarne Amstrup, Niels Woetmann Nielsen and Bent Hansen Sass: DMI-HIRLAM parallel tests with upstream and centered difference advection of the moisture variables for a summer and winter period in 2002

No. 03-04

Alexander Mahura, Dan Jaffe and Joyce Harris: Identification of sources and long term trends for pollutants in the Arctic using isentropic trajectory analysis

No. 03-05

Jakob Grove-Rasmussen: Atmospheric Water Vapour Detection using Satellite GPS Profiling

No. 03-06

Bjarne Amstrup: Impact of NOAA16 and NOAA17 ATOVS AMSU-A radiance data in the DMI-HIRLAM 3D-VAR analysis and forecasting system - January and February 2003

No. 03-07

Kai Sattler and Henrik Feddersen: An European Flood Forecasting System EFFS. Treatment of uncertainties in the prediction of heavy rainfall using different ensemble approaches with DMI-HIRLAM

No. 03-08

Peter Thejll and Torben Schmith: Limitations on regression analysis due to serially correlated residuals: Application to climate reconstruction from proxies

No. 03-09

Peter Stauning, Hermann Lühr, Pascale Ultré-Guérard, John LaBrecque, Michael Purucker, Fritz Prindahl, John L. Jørgensen, Freddy Christiansen, Per Høeg, Kent B. Lauritsen:

OIST-4 Proceedings. 4th Oersted International Science Team Conference. Copenhagen 23-27 September 2002

No. 03-10

Niels Woetmann Nielsen: A note on the sea surface momentum roughness length.

No. 03-11

Niels Woetmann Nielsen: Quasigeostrophic interpretation of extratropical cyclogenesis